Temperature and concentration dependence of the effective pair interaction parameters in Ni-Pd from high-energy x-ray diffuse scattering

M. Mezger,[1,*] H. Reichert,[1,†] I. B. Ramsteiner,[1] A. Udyansky,[1] O. Shchyglo,[1] V. N. Bugaev,[1]
H. Dosch,[1,2] and V. Honkimäki[3]
[1]*Max-Planck-Institut für Metallforschung, Heisenbergstrasse 3, D-70569 Stuttgart, Germany*
[2]*Institut für Theoretische und Angewandte Physik,Universität Stuttgart, Pfaffenwaldring 57, D-70550 Stuttgart, Germany*
[3]*European Synchrotron Radiation Facility, F-38043 Grenoble, France*
(Received 16 February 2006; published 31 May 2006)

The atomic interaction potential between different alloy components is encoded in the diffuse scattering caused by configurational short-range order and lattice distortions in the disordered phase. We performed *in situ* measurements of the x-ray diffuse scattering on macroscopic $Ni_{55}Pd_{45}$ and $Ni_{25}Pd_{75}$ single crystals in the temperature range from 20 °C up to 920 °C. We describe in detail the experiments and the data analysis where we use a formalism based on the spherical model and the Kanzaki-force concept in combination with a simulated annealing algorithm. We demonstrate that one single measurement is sufficient to retrieve the effective pair interaction potentials as well as thermal and elastic properties of the system. With only seven independent and physically motivated parameters we are able to describe short-range-order correlations, lattice distortions, and thermal parameters in a large temperature and concentration range.

DOI: 10.1103/PhysRevB.73.184206 PACS number(s): 61.66.Dk, 64.60.Cn, 34.20.Cf, 05.50.+q

I. INTRODUCTION

Effective interaction potentials are most important quantities in order to describe the structure of multicomponent systems.[1] Since local deviations of the system from the average structure are determined by the balance of the thermal energy and the free energy of the system, detailed knowledge of the fluctuation spectrum allows one to reconstruct the underlying effective interaction potential.[2,3] Diffuse x-ray and neutron scattering measurements are ideal tools to sample these fluctuations and their dispersion.

With the fast increase in computing resources, first-principles calculations of the structure of alloys are now performed routinely.[4] A critical testbed for the resulting alloy models is then the diffuse scattering of x rays and neutrons.[5] In particular, calculated short-range-order (SRO) maps are compared with measurements of the diffuse scattering from the real alloy systems.[6,7] On the other hand, collecting and analyzing diffuse scattering data still remains a tedious task despite the explosive development of x-ray sources during the last two decades. Therefore, the number of available experimental data sets is limited. In this work we demonstrate that new approaches based on the use of high-energy x rays[8] and a reciprocal-space description of diffuse scattering[9] now enable us to determine interaction parameters of real systems very efficiently.

Traditionally, diffuse scattering distributions have been measured in reflection geometry with point detectors employing x rays at moderate energies ($E \approx 10$ keV).[10] By using high-energy x rays ($E \approx 100$ keV) from third-generation synchrotron sources in transmission geometry and in combination with two-dimensional (2D) area detectors, we now gain orders of magnitude in data quality and time resolution.[7,8] Similar to transmission electron microscopy the large radius of the Ewald sphere allows one to map planes in reciprocal space in high-energy x-ray diffraction experiments with a single exposure. Due to the large penetration depth of high-energy x rays, large sample volumes can be illuminated to produce large diffuse scattering signals, even though the underlying diffuse scattering cross section is very small.

In parallel, we have also developed a reciprocal-space description for local compositional fluctuations in a single unified model which allows one to analyze the diffuse scattering data in terms of a few physically motivated parameters.[9] In this work we demonstrate that the parameters of this model can be determined with high accuracy from high-energy diffraction data.

The alloy system Ni-Pd is an ideal candidate for a systematic study of the temperature and concentration dependence of fundamental alloy properties. Ni and Pd form a continuous solid solution over the entire composition range without any ordered or intermetallic phases. The large atomic size mismatch between Ni and Pd of about 10% is indicative of large internal strain effects with significant distortion-induced contributions to the diffuse scattering pattern. Since the average form factor and the contrast between Ni and Pd are of the same order, it is possible to disentangle the chemical and strain-induced parts of the interaction potential. To demonstrate the capabilities of the methods, we have measured and analyzed the diffuse scattering intensity distributions in Ni-Pd alloys in order to study the configurational disorder in the system.

In Sec. II we summarize the theoretical model for the description of the diffuse scattering. All components of the diffuse scattering are described within a unified reciprocal-space model using a single parameter set. The alloy system Ni-Pd and some of its properties are then introduced in Sec. III. After summarizing the experimental approach and a qualitative discussion of the measured data sets in Sec. IV, we demonstrate the full data analysis from a single diffuse scattering pattern in Sec. V, before we discuss the final results of the data analysis for $Ni_{55}Pd_{45}$ and $Ni_{25}Pd_{75}$ in Sec. VI, with particular emphasis on the temperature dependence of the results. Section VII concludes with a discussion of the

 ©2006 The American Physical Society

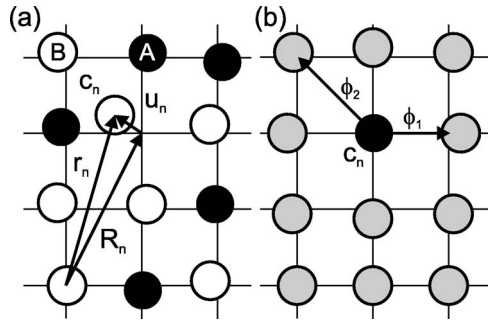

FIG. 1. Configuration of a binary alloy system. (a) The system is totally described by N occupation numbers $c_n = c_{\boldsymbol{R}_n}$ and N inhomogeneous lattice distortions $\boldsymbol{u}_n$ from the ideal lattice positions $\boldsymbol{R}_n$. (b) The lattice distortions are modeled by shell dependent Kanzaki forces ϕ_s.

capabilities of our methods for measuring and analyzing diffuse scattering patterns of binary alloys.

II. THEORY

A. Hamiltonian of binary alloys

The configuration of a binary mixture A_cB_{1-c} of A and B atoms on a periodic lattice is described by the occupation numbers

$$c_n = c_{\boldsymbol{R}_n} = \begin{cases} 1, & A \text{ atom on site } \boldsymbol{R}_n, \\ 0, & \text{otherwise}, \end{cases} \tag{1}$$

with $n=1,\ldots,N$ (N denotes the number of lattice sites). In addition there are continuous degrees of freedom for the lattice distortions $\boldsymbol{u}_n$ [see Fig. 1(a)]. In the quasiharmonic approximation,[3,11] the Hamiltonian $H^{\mathrm{tot}}(\{c_n,\boldsymbol{u}_n\})$ can be split into a chemical part $H^{\mathrm{ch}}(\{c_n\})$ and a strain-induced part $H^{\mathrm{si}}(\{c_n,\boldsymbol{u}_n\})$,

$$H^{\mathrm{tot}}(\{c_n,\boldsymbol{u}_n\}) = H^{\mathrm{ch}}(\{c_n\}) + H^{\mathrm{si}}(\{c_n,\boldsymbol{u}_n\}). \tag{2}$$

Since the lattice distortions are depending on the local chemical environment, H^{si} is a function of $\boldsymbol{u}_n$ and c_n. In the following we describe a model with only a few system-dependent parameters to model the functions H^{ch} and H^{si}.

The chemical part of the Hamiltonian $H^{\mathrm{ch}}(\{c_n\})$ can be described in the pair approximation by

$$H^{\mathrm{ch}}(\{c_k\}) = H^{(0)} + cNV^{\mathrm{ch}(1)} + \frac{1}{2}\sum_{\boldsymbol{k}} V_{\boldsymbol{k}}^{\mathrm{ch}(2)} c_{\boldsymbol{k}} c_{\boldsymbol{k}}^*, \tag{3}$$

with $H^{(0)}$ denoting the configuration-independent part and $V^{\mathrm{ch}(1)}$ the so-called injection energy of atom A into the unrelaxed matrix. $V_{\boldsymbol{k}}^{\mathrm{ch}(2)}$ and $c_{\boldsymbol{k}}$ are the Fourier transforms of the two-body mixing energy and the occupation numbers, respectively. Using Eq. (3) the many-body interactions are projected onto effective two-body interaction parameters $V^{\mathrm{ch}(2)}$ which in turn become concentration dependent.

In order to develop an efficient model for the strain-induced part of the Hamiltonian, a Kanzaki force concept is employed.[1,12] In this model the long-range distortions are caused by Kanzaki forces ϕ_s on the s-neighbor shells $s=1,2,\ldots$ [see Fig. 1(b)], where the forces ϕ_1 and ϕ_2 act on the "gray" atoms in the nearest- and next-nearest-neighbor shells, respectively, producing via superposition the lattice distortions depicted in Fig. 1(a). To second order the Fourier transform of H^{si} is then described by

$$H^{\mathrm{si}}(\{c_k\}) = cNV^{\mathrm{si}(1)} + \frac{1}{2}\sum_{\boldsymbol{k}} V_{\boldsymbol{k}}^{\mathrm{si}(2)} c_{\boldsymbol{k}} c_{\boldsymbol{k}}^*, \tag{4}$$

where $V^{\mathrm{si}(1)}$ describes the strain-induced part of the injection energy.[3] The correctly normalized strain-induced pair interaction potential $V_{\boldsymbol{k}}^{\mathrm{si}(2)}$ is given by

$$V_{\boldsymbol{k}\neq 0}^{\mathrm{si}(2)} = -\phi_{\boldsymbol{k}}^{+}\mathsf{G}_{\boldsymbol{k}}\phi_{\boldsymbol{k}} + \frac{1}{N}\sum_{\boldsymbol{k}\neq 0}\phi_{\boldsymbol{k}}^{+}\mathsf{G}_{\boldsymbol{k}}\phi_{\boldsymbol{k}}, \tag{5}$$

with $\mathsf{G}_{\boldsymbol{k}}$ the lattice Green's function, $c_{\boldsymbol{k}}$ the concentration waves, and $\phi_{\boldsymbol{k}}$ the Fourier transform of the Kanzaki force. The lattice Green's function and the Kanzaki forces used for this work are given in the Appendix. Note that the Fourier transform $\boldsymbol{u}_n$ is given by[9]

$$\boldsymbol{u}_{\boldsymbol{k}} = \mathsf{G}_{\boldsymbol{k}}\phi_{\boldsymbol{k}}c_{\boldsymbol{k}}. \tag{6}$$

In the continuum limit the change of the lattice constant a is related to the Kanzaki forces ϕ_S on shell s and the elastic constants c_{ij} (Ref. 1):

$$L = \frac{1}{a}\frac{\partial a}{\partial c} = \frac{1}{3v_0(c_{11}+2c_{12})}\sum_{\boldsymbol{R}_s} \boldsymbol{R}_s \cdot \phi_s, \tag{7}$$

where v_0 denotes the volume of the unit cell and $\boldsymbol{R}_s$ the atomic positions in the interaction shell S.

B. Short-range order of binary alloys

The configurational short-range order in binary systems is most conveniently characterized by the SRO parameters $\alpha_{\boldsymbol{k}}$ which are related to the correlation function $\epsilon_{\boldsymbol{k}} = c(1-c)\alpha_{\boldsymbol{k}}$. Within the spherical model approximation $\alpha_{\boldsymbol{k}}$ can be calculated by[13]

$$\alpha_{\boldsymbol{k}} = \frac{1}{1 + c(1-c)\beta W_{\boldsymbol{k}}^{\mathrm{tot}}}. \tag{8}$$

For a correct normalization of the SRO parameters a Lagrangian multiplier λ is introduced:[14]

$$W_{\boldsymbol{k}} = V_{\boldsymbol{k}}^{\mathrm{ch}(2)} + V_{\boldsymbol{k}}^{\mathrm{si}(2)} + \lambda. \tag{9}$$

The parameter λ must be determined numerically by integrating $\alpha_{\boldsymbol{k}}$ over the Brillouin zone $\mathcal{B}$ and the boundary condition $1 = \alpha_{000} = \Sigma_{\boldsymbol{k}\neq 0}\alpha_{\boldsymbol{k}}$. While in the past a variety of other normalization procedures have been described in the literature,[15] Eq. (9) provides highly accurate results, in particular close to phase transformations at lower temperatures.

C. X-ray diffuse scattering

Local deviations from the average lattice caused by concentration fluctuations and lattice distortions give rise to diffuse scattering

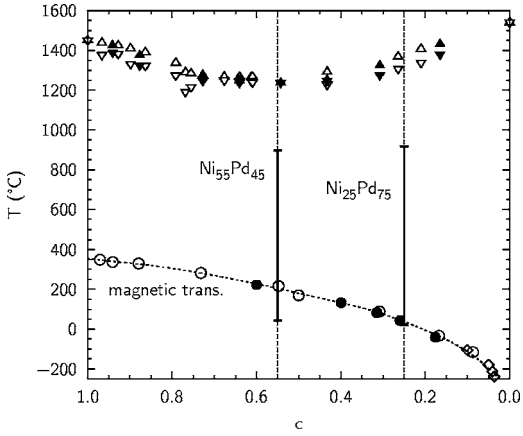

FIG. 2. Ni_cPd_{1-c} phase diagram.

$$A_{\mathrm{diff}}(\boldsymbol{q}) = \sum_{n=1}^{N} f_n(\boldsymbol{q}) e^{i\boldsymbol{q}\cdot(\boldsymbol{R}_n+\boldsymbol{u}_n)} - \bar{f}(\boldsymbol{q}) \sum_{n=1}^{N} e^{i\boldsymbol{q}\cdot\boldsymbol{R}_n}, \tag{10}$$

with $\bar{f}=cf_A+(1-c)f_B$ denoting the average x-ray form factor and $\boldsymbol{q}$ the momentum transfer. Assuming small lattice distortions $\boldsymbol{u}_n$, the diffuse scattering intensity is given by

$$I_{\mathrm{diff}}(\boldsymbol{q}) \propto e^{-2B_{\mathrm{th}}q^2}[I_{\mathrm{DS}}(\boldsymbol{q}) + I_{\mathrm{TDS}}(\boldsymbol{q})], \tag{11}$$

with the Debye-Waller factor $D_W=e^{-2B_{\mathrm{th}}q^2}$. Here $2B_{\mathrm{th}}$ denotes the well-known thermal Debye parameter.[16] The diffuse scattering due to SRO and static lattice distortions I_{DS} is finally given by[1–3]

$$I_{\mathrm{DS}}(\boldsymbol{q}) \propto \langle |\Delta c_{\boldsymbol{q}} + i\bar{f}\boldsymbol{q}\cdot\boldsymbol{u}_{\boldsymbol{q}}|^2 \rangle \tag{12a}$$

$$\propto \alpha_{\boldsymbol{q}}(\Delta f - \bar{f}\boldsymbol{q}^{+}\mathsf{G}_{\boldsymbol{q}}\phi_{\boldsymbol{q}})^2, \tag{12b}$$

where we have used the SRO parameters $\alpha_{\boldsymbol{q}}$ to replace the static lattice distortions and the correlation function $\epsilon_{\boldsymbol{k}}$. The thermal diffuse scattering I_{TDS} due to lattice vibrations is taken into account within the same formalism by

$$I_{\mathrm{TDS}}(\boldsymbol{q}) \propto \bar{f}^2 k_{\mathrm{B}} T \boldsymbol{q}^{+}\mathsf{G}_{\boldsymbol{q}}\boldsymbol{q}. \tag{13}$$

Note that Eq. (13) includes first-order thermal diffuse scattering only (single-phonon processes).

III. Ni-Pd ALLOY SYSTEM

Figure 2 depicts the Ni-Pd phase diagram as compiled from various sources.[17–21] Fraenkel and Stern[18] found the eutectic concentration at approximately 60 wt % palladium which corresponds to the composition $Ni_{55}Pd_{45}$. The Ni-Pd system forms a homogeneous solid fcc solution in the entire concentration range without any ordered or intermetallic phases. At low temperatures a ferromagnetic phase is formed in a large concentration range with a Curie temperature below 627 K. In measurements of the electric conductivity,[22] hints for an irregular behavior near the composition $Ni_{25}Pd_{75}$ were found. Bingham and Brooks[23] and Tomiska *et al.*[24] found anomalies in heat capacity measurements close to a temperature of 700 K and well above the Curie temperature. These features were especially pronounced for stoichiometric and palladium-rich alloys and explained by a loss of chemical short-range order. The vertical lines in Fig. 2 for the eutectic compositions $Ni_{55}Pd_{45}$ and $Ni_{25}Pd_{75}$ represent the two concentrations and the temperature range where our measurements were performed.

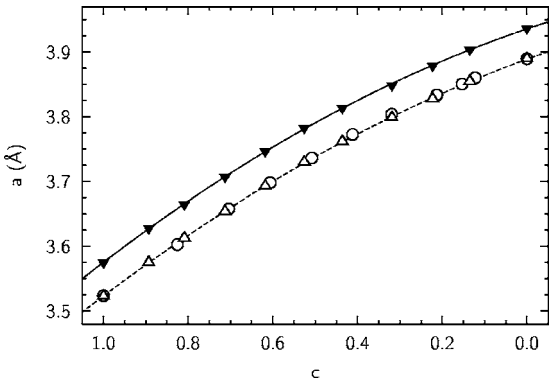

FIG. 3. Lattice parameters of Ni_cPd_{1-c} alloys at 25 °C (open circles and triangles) and 900 °C (solid triangles) taken from the literature (Refs. 25 and 26).

In order to take full advantage of Eq. (7) for the calculation of the Kanzaki forces, $\partial a/\partial c$ and the bulk modulus $K=\frac{1}{3}(c_{11}+2c_{12})$ must be known. Figure 3 shows the lattice parameters of Ni_cPd_{1-c} alloys compiled from data sets by Pownceby and O'Neil[25] and Bidwell and Speiser[26] together with quadratic interpolations. From these parameters the lattice constants a, the parameters $L=(a_1+a_2c)/a$, and the linear thermal expansion $\Delta a/\Delta T$ can be calculated for the compositions $c=0.25$ and $c=0.55$ used in this work (see Table I).

Experimentally the bulk modulus K of polycrystalline Ni-Pd samples was measured by Joshihara and McLellan[27] as a function of concentration and temperature. Figure 4 shows interpolated data for $c=0.55$ and $c=0.25$ together with linear interpolations for the temperature dependence in the range from 350 °C to 900 °C, where we performed quantitative scattering experiments.

IV. EXPERIMENTS

A. Sample preparation and characterization

Single crystals of the $Ni_{25}Pd_{75}$ and the eutectic concentration $Ni_{55}Pd_{45}$ were grown by the Bridgeman technique. The $Ni_{55}Pd_{45}$ crystal was additionally refined by zone melting. Using spark erosion cylindrical crystal rods with 8 mm diameter were cut in slices of 1 mm thickness with the surface

TABLE I. Lattice constant a, L, and linear thermal expansion $\Delta a/\Delta T$ for $c=0.25$ and $c=0.55$.

	a (25 °C) (Å)	L (25 °C)	$\Delta a/\Delta T$ (10^{-5} Å K^{-1})
$Ni_{25}Pd_{75}$	3.822	−0.07908	5.775
$Ni_{55}Pd_{45}$	3.720	−0.1018	6.033

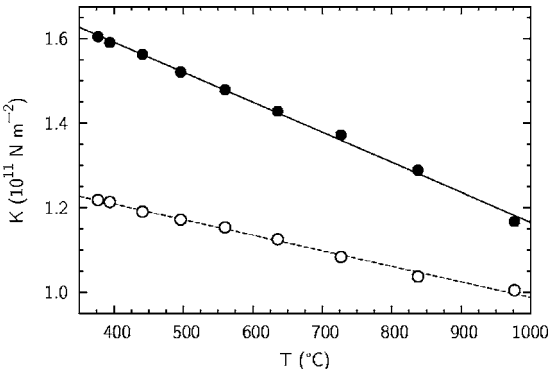

FIG. 4. Bulk modulus K of $Ni_{55}Pd_{45}$ (solid circles) and $Ni_{25}Pd_{75}$ (open circles) alloys for various temperatures extracted from Yoshihara and McLellan (Ref. 27) and linear interpolation (straight lines).

normal oriented in the (100) direction. The disk-shaped samples were polished with diamond paste (grain size 1 μm) and subsequently etched in hydrochloric acid kept at $T=70\,^{\circ}$C with a small amount of nitric acid. Since the experiments were performed on thick bulk samples in transmission geometry, details of the sample surface morphology are irrelevant. The final thickness d_0 of the samples is summarized in Table II.

Prior to the experiments the samples were annealed at 950 °C for 6 h. The crystallinity of the samples was determined by rocking scans in a ^{137}Cs γ-diffractometer at an energy of $E=661.65$ keV. The full width at half maximum (FWHM) of the (200) Bragg reflection was determined to be 0.3° for $Ni_{25}Pd_{75}$ and 0.05° for the zone molten $Ni_{55}Pd_{45}$ sample. The concentrations deduced from the x-ray fluorescence analysis are listed in Table III and show good agreement with the nominal values.

B. X-ray measurements

The x-ray diffuse scattering experiments were performed at the European Synchrotron Radiation Facility (ESRF) at the high-energy beamline ID15A. The energy of the x rays of 76.5 keV with a resolution of $\Delta E/E=2\times10^{-3}$ was calibrated at the Au K-edge at 80.7 keV.

The experimental setup used in this work is sketched in Fig. 5. A monochromatic beam with a cross section of 0.5 mm$\times$0.5 mm transmits a monitor diode before entering a stationary vacuum chamber with a crystalline Si window. The parasitic scattering from the Si window was removed by an adjustable pinhole in front of the sample. During the experiments the sample chamber was evacuated to a pressure of 10^{-6} mbar in order to reduce the background from air scattering and avoid oxidation of the sample at high temperature. Note that the small oxidation during the experiments produces only nanometer-sized oxide layers which do not contribute measurably to the diffuse scattering patterns. The samples were mounted on a BN heating stage with a central hole in order to perform *in situ* scattering experiments in transmission geometry between room temperature and 1000 °C. The sample temperature was measured using a NiCr/Ni thermocouple.

TABLE II. Thickness d_0, transmission T, and optimal thickness d_{opt} calculated for the x-ray energy $E=76.5$ keV. The effective thickness d_{eff} has been determined using Eq. (15).

	d_0	d_{opt}	$d_{eff}\,(\theta=0)$	T
$Ni_{25}Pd_{75}$	420 μm	358 μm	130 μm	0.31
$Ni_{55}Pd_{45}$	480 μm	484 μm	180 μm	0.37

TABLE III. Results of the chemical analysis (XRF).

	Mass % Ni	Mass % Pd	at. % Ni	at. % Pd
$Ni_{55}Pd_{45}$	39.85±0.20	59.99±0.30	54.7	45.3
$Ni_{25}Pd_{75}$	15.61±0.07	84.55±0.40	25.0	75.0

The orientation of the sample relative to the incoming x-ray beam was adjusted by two motorized tilt angles ϕ and χ. In addition, the sample assembly could be rotated in the beam by $\omega=\pm52°$. The scattered intensity was recorded with a two-dimensional online image plate reader (mar345) with 2300×2300 pixels at a pixel size of 150 μm. Using a 2-mm-thick Al exit window enabled us to remove low-energy fluorescence background scattering from the sample. This setup allows us to record high-quality diffuse scattering data with approximately 100 s counting time for each orientation of the Ni-Pd samples. The exact sample to detector distance $D=845$ mm was determined from the radii of Fe powder rings recorded from a standard Fe powder sample. Using high-energy x rays and a two-dimensional detector in this configuration we could map diffuse scattering patterns up to 4.5 reciprocal lattice units from our Ni-Pd alloy crystals.

Each recorded pixel (i,j) on the 2D detector corresponds to a distinct scattering vector $\boldsymbol{q}=(q_x,q_y,q_z)$ which can be calculated by

$$q_x^{ij}=R[\cos(\omega)\gamma_{ij}i-\sin(\omega)(1-\gamma_{ij}\beta)], \tag{14a}$$

$$q_y^{ij}=R\gamma_{ij}j, \tag{14b}$$

$$q_z^{ij}=R[\sin(\omega)\gamma_{ij}i+\cos(\omega)(1-\gamma_{ij}\beta)], \tag{14c}$$

$$R=\frac{a}{\lambda},\quad \beta=\frac{D}{\delta},\quad \gamma_{ij}=(\beta^2+i^2+j^2)^{-1/2}. \tag{14d}$$

δ denotes the pixel size, a the lattice constant, λ the x-ray wavelength, and i,j the pixel coordinates on the detector relative to the point were the primary beam hits the detector. Due to the short x-ray wavelength $\lambda\ll a$, the q_x and q_y components are almost straight lines, which allows a straightforward qualitative interpretation of the diffraction pattern. Figure 6 shows the indexation diagram for the sample orientation $\omega=0$ and the (001) sample surface normal parallel to the incoming beam. For this orientation the concentric lines denote lines of constant l in reciprocal space, while the slightly distorted mesh depicts the in-plane indices h and k in the (h,k) plane.

In situ scattering experiments were performed at different

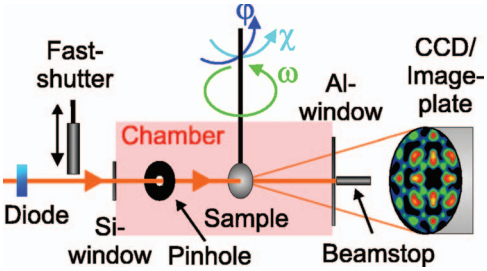

FIG. 5. (Color) Setup for the high-energy x-ray scattering experiments in Laue geometry.

temperatures between room temperature and 920 °C. Due to the large dynamic range of the x-ray diffuse scattering, the intensity patterns were determined with two exposures, where during the second exposure additional Pb absorbers were mounted on the image plate near the positions where large intensities occur. Combining the data sets measured with and without the Pb absorbers results in diffuse scattering maps with superior statistics over the entire intensity range.

In addition we have explored the diffuse scattering distribution in 3D reciprocal space at room temperature by recording individual scattering patterns while rotating the samples around ω in steps of $\Delta\omega=1°$. A qualitative analysis confirmed that the most prominent diffuse scattering features appear in high-symmetry planes.

Figure 7 shows experimentally measured scattering patterns with the (100) sample surface normal ($\omega=0°$) oriented along the incident beam. At high temperatures (right) the intensity distribution is dominated by thermal diffuse scattering (TDS) which is mainly concentrated around the positions of bulk Bragg reflections and along the {1,1,0} soft-phonon high-symmetry directions. At room temperature, where the TDS is strongly reduced, diffuse peaks at the superstructure positions {110} and {310} are clearly visible. In addition, pronounced shoulders appear on the low-q side of bulk Bragg reflections along h and k directions.

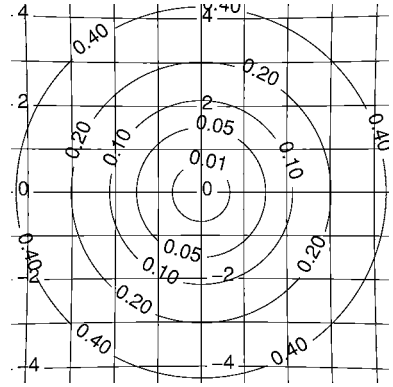

FIG. 6. Indexation diagram for the $Ni_{55}Pd_{45}$ sample and the setup used in this work (lattice constant $a=3.72$ Å, x-ray energy $E=76.5$ keV, detector distance $D=845$ mm). The sample orientation is $\omega=0$.

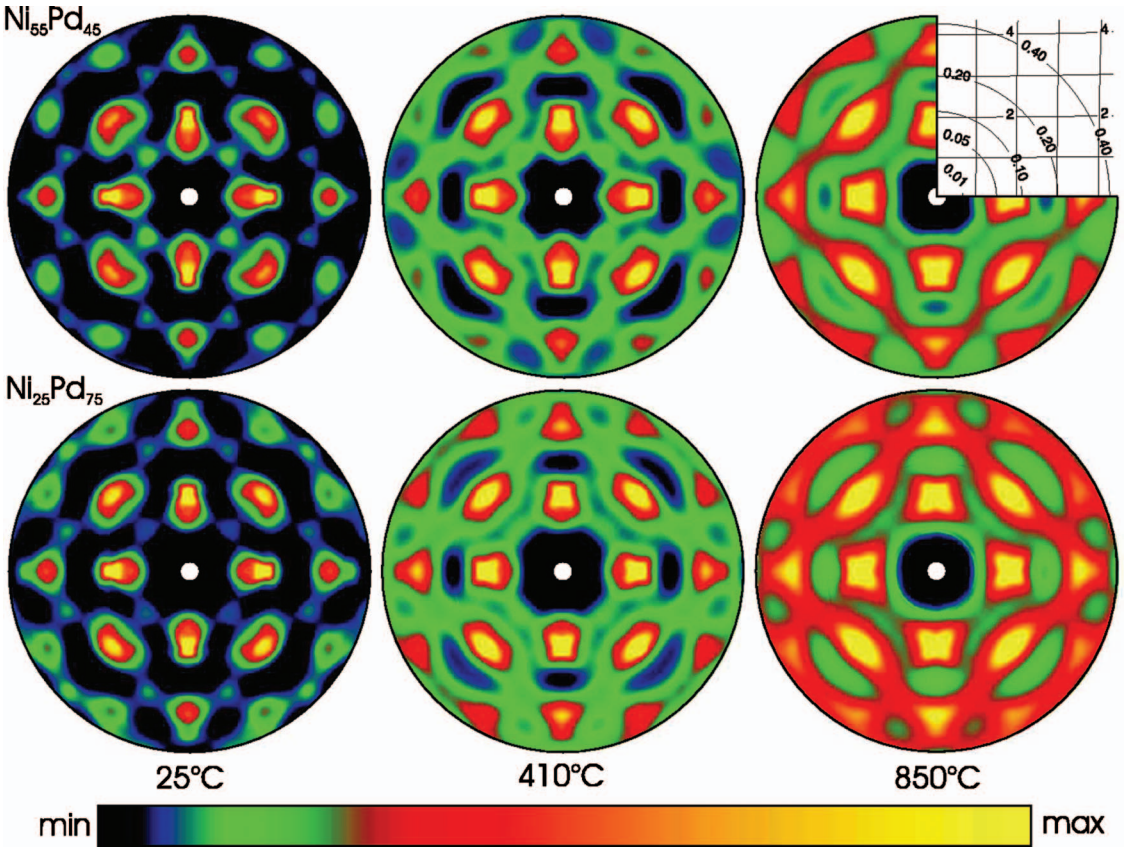

FIG. 7. (Color) Diffuse x-ray intensities from $Ni_{55}Pd_{45}$ (upper row) and $Ni_{25}Pd_{75}$ (lower row) alloys at room temperature (left column), 410 °C (center column), and 850 °C (right column).

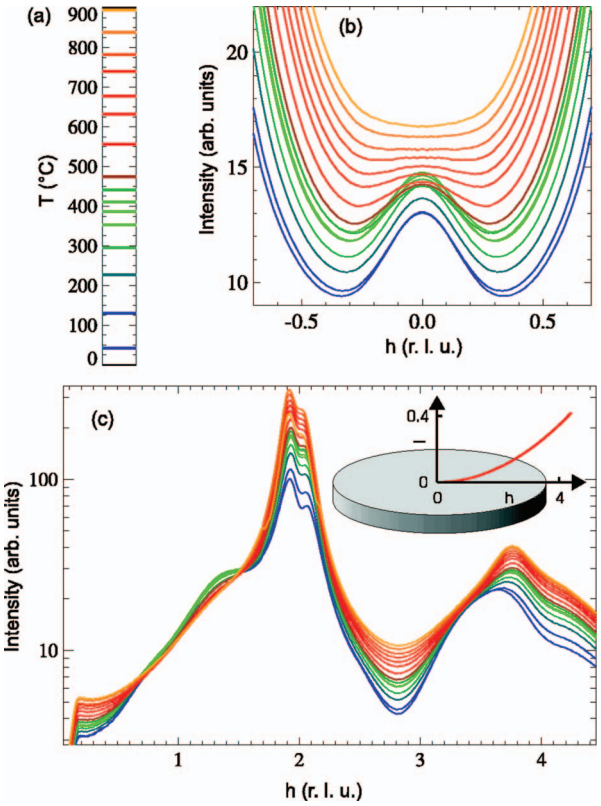

FIG. 8. (Color) Line scans of the diffuse intensity of $Ni_{55}Pd_{45}$ along (b) the $\langle 1+h,1-h,l(h)\rangle$ and (c) the $\langle h,0,l(h)\rangle$ direction as a function of temperature T. The temperatures are indicated on the scale bar (a). The inset in (c) sketches the line scan in the $(h,0,l)$ plane.

Figure 8 shows in more detail symmetry-averaged line scans through the prominent diffuse scattering features in Fig. 7. The diffuse scattering maximum centered at (1,1,0.044) and its temperature dependence are displayed in Fig. 8(b) along the line $(1+h,1-h,l(h))$. At higher temperatures the peak is decreasing and buried by the increasing TDS. The temperature dependence of the pronounced shoulder at $h=1.4$, close to the (200) Bragg reflection, is shown in Fig. 8(c) along the line $(h,0,l(h))$. Since the diffraction pattern is recorded on a curved Ewald sphere with $l\neq 0$ except for the origin, the scattered intensity does not directly intersect the fcc Bragg peaks. The TDS streaks along the high-symmetry directions emanating from the Bragg reflections appear as split asymmetric peaks around the positions $(h=2,0,0.087)$ and $(h=4,0,0.35)$.

The principal features in the diffuse scattering patterns for both concentrations are very similar. This is shown in Fig. 9 where the line scans along $(h,0,l(h))$ are shown for both concentrations at room temperature.

After each temperature change, the scattered intensity was monitored to determine when the system equilibrated. Because the diffusion of Ni and Pd atoms is strongly temperature dependent, it is the rate limiting process for configurational changes in the alloy samples and prevents equilibrium states from being reached at low temperatures. In order to estimate the temperature where the samples did not reach

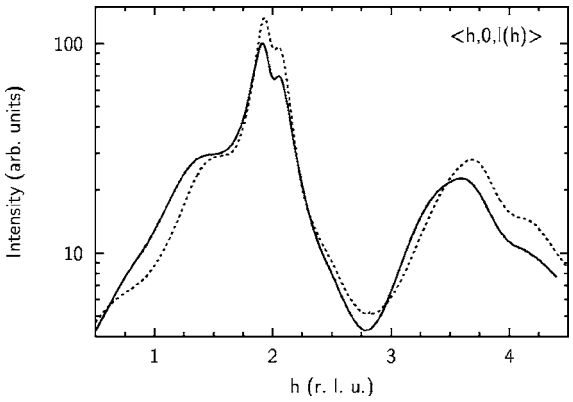

FIG. 9. Diffuse x-ray intensity from $Ni_{55}Pd_{45}$ (solid line) and $Ni_{25}Pd_{75}$ (dashed line) along $(h,0,l(h))$ at room temperature.

equilibrium at time scales accessible in *in situ* synchrotron radiation experiments, we have monitored the diffuse superstructure intensities as a function of temperature. Figure 10 shows the integrated intensity of the diffuse scattering maximum centered at (1,1,0.045) for the two different samples. Surprisingly, a sharp kink with a distinct change in slope is clearly visible for $Ni_{55}Pd_{45}$ at 350 °C with the diffuse scattering remaining almost constant below this temperature. Since the diffuse scattering peak centered at (1,1,0.045) is a clear signature of ordering fluctuations in the system, the chemical SRO appears to be frozen below $T=350$ °C which is very close to the magnetic phase transformation. This behavior suggests that the chemical and magnetic structures are intimately related in the Ni-Pd system. The kink at 350 °C is weaker for $Ni_{25}Pd_{75}$ but still present. Since the origin of this phenomenon is presently unclear, we have limited the quantitative analysis of the diffuse scattering patterns to temperatures above 350 °C.

V. DATA ANALYSIS

A. Raw data correction

The raw intensity patterns were first scaled to the intensity of the incident beam recorded by the diode. Subsequently, background intensity patterns measured without a sample in

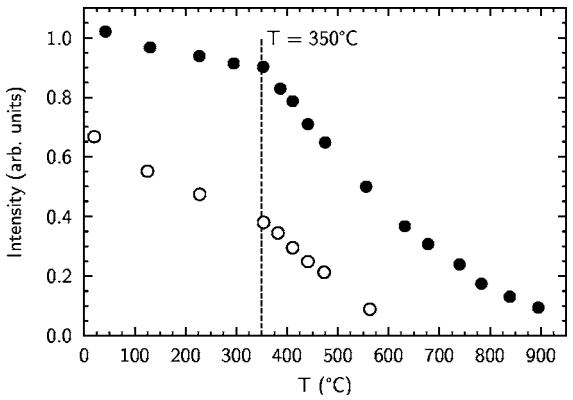

FIG. 10. Integrated intensity of the diffuse {110} superlattice peak for $Ni_{55}Pd_{45}$ (solid circles) and $Ni_{25}Pd_{75}$ (open circles).

the beam were subtracted from the raw images. In the next step the intensity patterns were corrected for absorption effects. This is taken into account by the effective sample thickness d_{eff}, which depends on the scattering angle 2θ,

$$d_{eff} = d_0 e^{-\mu d_0} \frac{(e^{\mu d_0(1-1/\beta\gamma_{ij})} - 1)}{\mu d_0(1 - 1/\beta\gamma_{ij})}, \tag{15}$$

with μ denoting the absorption coefficient. The highest intensity can be achieved for a scattering angle of $2\theta=0$ at an optimum sample thickness of $d_{opt}=\mu^{-1}$. For the samples used in this work the sample thicknesses d, d_{opt}, and d_{eff} and the transmission at the actual sample thickness T are summarized in Table II. The measured intensity patterns were finally normalized to the optimum sample thickness d_{opt}.

For a quantitative analysis of the diffuse scattering patterns several geometrical correction factors have to be taken into account. The first correction takes into account the different solid angles $\Delta\Omega_{ij}$ recorded at each detector pixel coordinate i,j. The corresponding solid angle can be calculated by integrating the angular range $(\Delta_{2\theta}, \Delta_{\varphi})$ covered by each detector pixel. In spherical coordinates $\Delta\Omega_{ij}$ is given by

$$\Delta_{2\theta} = \frac{\delta \cos^2 2\theta}{D}, \tag{16a}$$

$$\Delta_{\varphi} = \frac{\delta \cos 2\theta}{\sin 2\theta D}, \tag{16b}$$

$$\Delta\Omega_{ij} \approx \beta^5 \gamma_{ij}^3. \tag{16c}$$

The second geometrical correction factor is induced by linear polarization of the synchrotron radiation in the horizontal plane. The corresponding correction factor in sperical coordinates is given by

$$P = \sin^2 \varphi + \cos^2 \varphi \cos^2 2\theta. \tag{17}$$

All the correction factors are very small owing to the high energy of the x-ray beam, which keeps the scattered intensity in a narrow angular range in the forward direction. Applying all the correction factors alters a measured intensity map by less than 4% across the entire image. Thus, just the raw diffuse scattering patterns give an excellent qualitative picture of the scattering cross section in reciprocal space.

B. Fitting procedure

For a quantitative comparison of the measured intensity distribution I^{exp} with the calculated intensities I^{cal} a cost function Δ has to be defined. Since the dynamic range of the measured diffuse scattering patterns exceeds two orders of magnitude, we have applied logarithmic scaling to the data. The overall cost function is then given by

$$\Delta = \sqrt{\langle \delta^2 \rangle - \langle \delta \rangle^2} \quad \text{with } \delta_{ij} = \ln \frac{I_{ij}^{\mathrm{cal}}}{I_{ij}^{\mathrm{exp}}}. \tag{18}$$

The data evaluation process can be divided in two steps. In the first step, a diffuse scattering pattern is calculated using the reciprocal-space formalism introduced in Sec. II and input parameters characterizing the specific alloy under consideration. In order to reproduce the measured diffuse scattering patterns, we have used nine independent physical parameters according to the model described in Sec. II.

(i) Three chemical interaction pair parameters $V_s^{\mathrm{ch}(2)}$.

(ii) One free coefficient φ for the ratio of the modulus of the Kanzaki forces in the first two neighboring shells; the two Kanzaki force parameters are then determined by the boundary condition defined in Eq. (7) (see the Appendix).

(iii) Two ratios of the elastic constants c_{12}/c_{11} and c_{44}/c_{11}; the absolute values of c_{11}, c_{12}, and c_{44} were then fixed by the bulk modulus K (see Fig. 4).

(iv) One thermal Debye parameter B_{th} for calculation of the thermal Debye-Waller factor D_W.

(v) Two parameters for an additional smooth background of parabolic shape.

This allows us to calculate the correlation function $\alpha_{\boldsymbol{k}}$ via the correctly normalized interaction parameters $V_{\boldsymbol{k}}$ including chemical and strain-induced components. The same set of parameters is used to calculate the distortion-induced part of the diffuse scattering pattern as well as the thermal diffuse scattering. In the second step a fitting routine is used to refine the independent model parameters of the alloy in order to reproduce the measured intensity distribution. For this purpose we have employed the adaptive simulated annealing (ASA) algorithm developed by Ingber.[28] Since the experimentally measured intensity maps contain redundant information due to the symmetry of the pattern, symmetry-averaged data sets have been used in the fitting procedure.

The use of a physically motivated model (see Sec. II) allows us to reduce the number of free fitting parameters by taking into account additional information, such as the derivative of the lattice constant a with respect to the alloy concentration c, which is related to the Kanzaki coefficients via Eq. (7) and the bulk modulus $K=\frac{1}{3}(c_{11}+2c_{12})$. This allows us to fix the absolute value of the elastic constants, which is especially important at high temperatures, where the scattered intensity is proportional to c_{ij}^{-1} for vanishing $\alpha_{\boldsymbol{q}}$.

C. Pattern analysis

By way of example we show the fitting results for $Ni_{55}Pd_{45}$ at the experimentally measured temperatures 410 °C and 900 °C. The pattern recorded at 410 °C is dominated by SRO and static lattice distortions, while the diffuse scattering pattern recorded at 900 °C is mainly caused by dynamic effects (TDS). The data points around the Bragg peaks (black) were not used for fitting in order to enhance sensitivity to the combined diffuse scattering from configurational SRO and distortion-induced scattering. Figure 11 shows that for both low and high temperatures, the calculated I^{cal} and measured I^{exp} intensities agree very well. This is a clear demonstration that the alloy model developed in Sec. II is capable of reproducing equally well configurational SRO, static, and dynamic lattice distortions by a single unified description.

Using the parameters determined in the fitting process the diffraction pattern can be calculated taking into account only the contribution of a certain part of Eq. (11). This serves as a

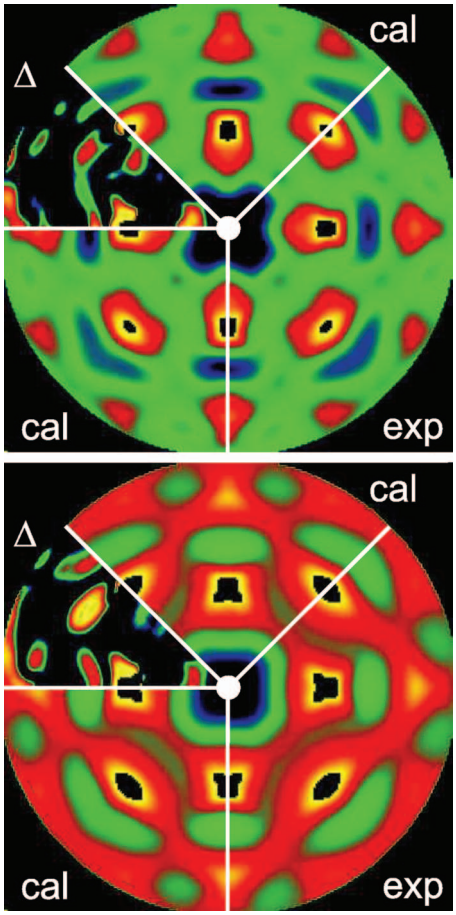

FIG. 11. (Color) Comparison of the calculated (cal) and the experimentally recorded (exp) diffraction pattern from $Ni_{55}Pd_{45}$ at 410 °C (top) and 900 °C (bottom). The differences Δ_{ij} calculated according to Eq. (18) are magnified in the upper left part of each pattern. Black areas have been masked and were not used for fitting.

tool to identify the source of individual components of the diffuse scattering. Figure 12 shows the calculated intensity contributions from thermal diffuse scattering TDS (left), distortion scattering (middle), and configurational SRO (left). The calculation was performed using all the parameters reproducing the experimental conditions and corresponds to a spherical cut through reciprocal space on the Ewald sphere. The individual components have been calculated by setting $\Delta f=0$ or $\bar{f}=0$, respectively.

Experimentally measured and calculated intensity patterns can now be compared and analyzed quantitatively. Figure 13 shows line scans along different directions in reciprocal space. The principal features of the diffuse scattering intensity distribution are very well reproduced. The unified description of the entire scattering pattern in a closed reciprocal-space formalism enables us to identify the origin of individual features. The diffuse scattering maxima located at $\{1,1,l\}$ and $\{3,1,l\}$ positions are caused by configurational SRO, while the pronounced shoulders on the low-q side of the (2,0,0) and (4,0,0) Bragg reflections are induced by static lattice distortions due to the size mismatch between Ni and Pd. The strongly peaking intensities close to the Bragg reflections are due to TDS.

In order to check the uniqueness of the results obtained by the procedure described above we have performed many tests of varying the total number of independent model parameters and starting values. Starting values were chosen within a range of one order of magnitude around the final values in order to check the stability of the results. By way of example, Fig. 14 shows the evolution of the chemical interaction parameter V_1 in the ASA process for ten independent runs using different starting values. Independent of the starting values, V_2 converges always to the same final value. The same excellent convergence is found for all of the other fitting parameters. This test provides strong evidence for the existence of a unique global minimum for this problem which can be found reproducibly by the ASA algorithm. Further tests, expanding and reducing the number of free model parameters, have been performed in order to confirm that the optimum number of independent model parameters have been chosen. The error bars for the individual model parameters were determined from many independent fitting cycles and define the lower boundary for error bars of the model parameters. Additional systematic errors are introduced by input parameters such as the bulk modulus K or experimental errors.

The model parameters were determined from experimental data recorded in a single high-symmetry pattern with the (100) axis parallel to the incident beam ($\omega=0$). For $Ni_{55}Pd_{45}$ we have recorded additional diffuse scattering patterns for a series of angles $-45° < \omega < 45°$ with $\Delta\omega=1°$ at room temperature. In Fig. 15 the measured room-temperature diffuse scattering pattern (top) in (110) orientation is compared with a calculated intensity map (bottom) using the fitting parameters $(V_S, \varphi, c_{ij}, a, b)$ obtained from the (100) diffuse scattering pattern measured at 350 °C, which is the temperature where the SRO is kinetically frozen. Although we did not use experimental data from the (110) orientation for the determination of the interaction parameters, all the important features of the diffuse intensity distribution coincide very well in the experimental and the calculated pattern. This surprising result originates from the fact that the two-dimensional diffuse scattering pattern was not recorded on a plane in

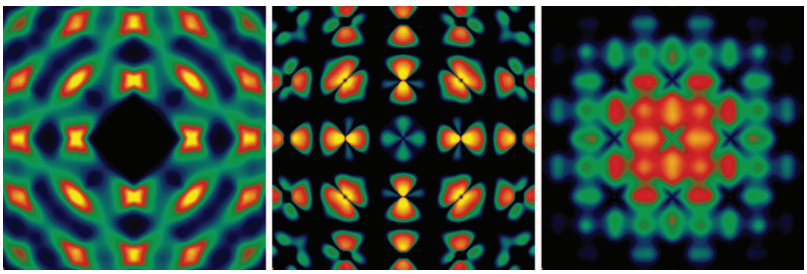

FIG. 12. (Color) Components of the diffuse scattering from $Ni_{55}Pd_{45}$ at 410 °C: TDS (left), distortion scattering (middle), and configurational SRO (left).

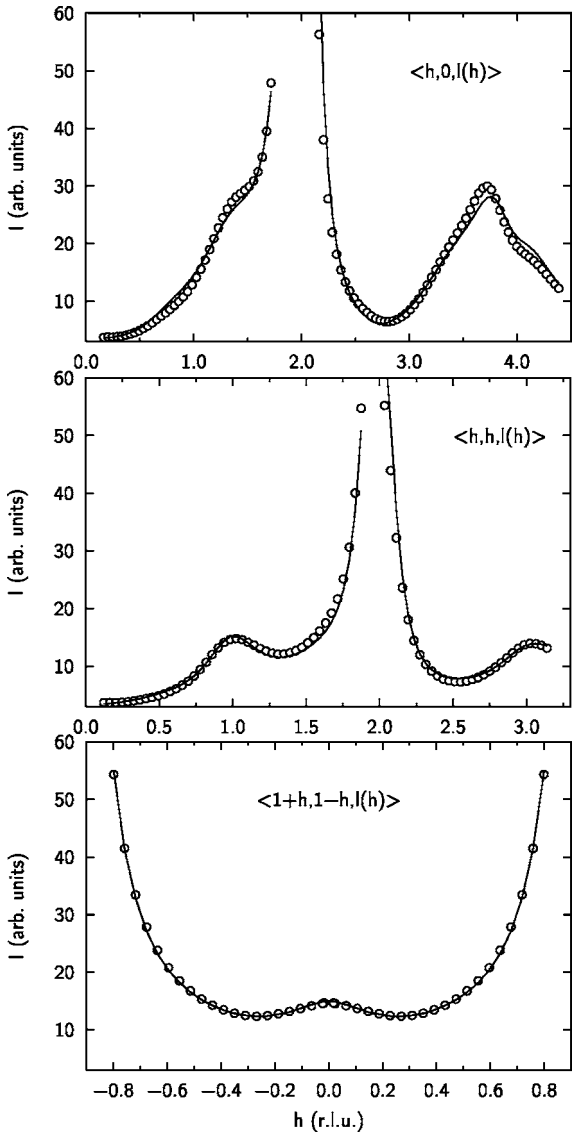

FIG. 13. Comparison of the calculated diffuse scattering intensities along selected lines in reciprocal space with measured data at T=410 °C for $Ni_{55}Pd_{45}$.

reciprocal space but on a sphere cutting through reciprocal space. The sphere cuts neighboring Brillouin zones in reciprocal space at different values of l [see Eq. (14)]. In this way, a single 2D data set contains 3D information which can be extracted with a suitable model such as the physically motivated reciprocal-space model introduced in Sec. II.

Using the procedures described above, we have analyzed a total of 23 experimentally measured data sets for $Ni_{55}Pd_{45}$ and $Ni_{25}Pd_{75}$ for a temperature range of 350 °C$<T<$920°C. In this temperature region the sample could be equilibrated on time scales accessible to *in situ* x-ray scattering experiments at synchrotron radiation facilities.

VI. RESULTS

The analysis of the diffuse scattering patterns has been performed completely independent for each temperature. In the following we discuss the resulting model parameters and their temperature dependence for both $Ni_{55}Pd_{45}$ and $Ni_{25}Pd_{75}$.

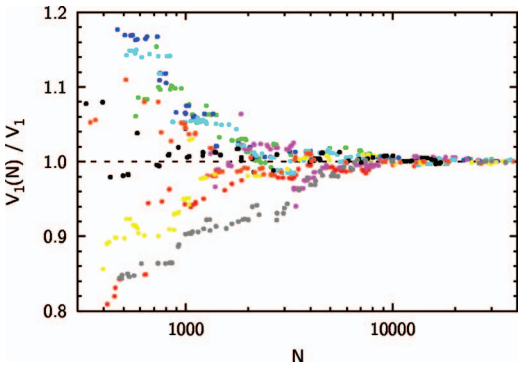

FIG. 14. (Color) Evolution of the chemical pair interaction parameter V_1 for different starting values in ten different ASA runs.

Figure 16 shows the chemical pair interaction parameters V_S as a function of temperature T. Although the diffuse intensity patterns change significantly from low to high temperature (see Fig. 7), the resulting chemical interaction pa-

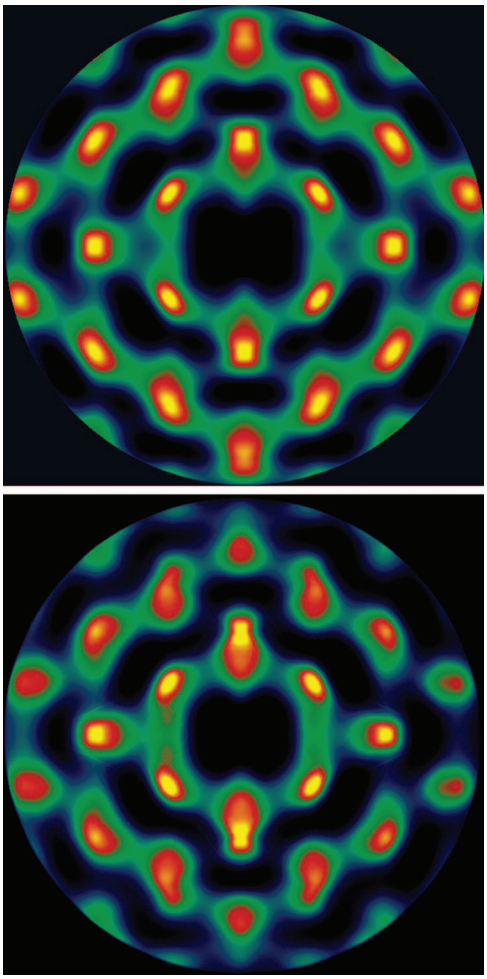

FIG. 15. (Color) Comparison of the calculated (top) and the experimental (bottom) diffuse scattering pattern from $Ni_{55}Pd_{45}$ at 25 °C in the (110) orientation.

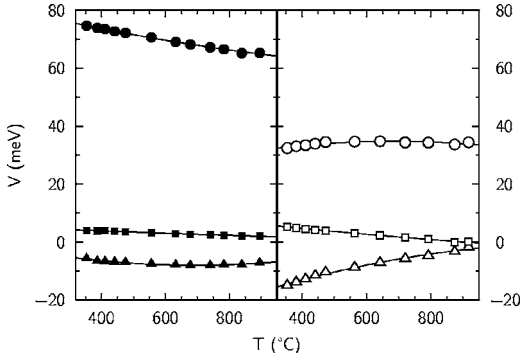

FIG. 16. Chemical pair interaction parameters V_1 (circles), V_2 (triangles), and V_3 (squares) obtained from fitting for the diffuse scattering patterns from $Ni_{55}Pd_{45}$ (left) and $Ni_{25}Pd_{75}$ (right). The lines are a guide for the eye.

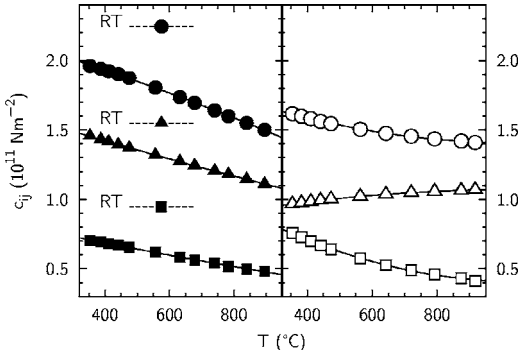

FIG. 17. Temperature-dependent elastic constants c_{11} (circles), c_{12} (triangles), and c_{44} (squares) for $Ni_{55}Pd_{45}$ (left) and $Ni_{25}Pd_{75}$ (right). The lines are a guide for the eye. Calclated room-temperature (RT) values are shown in the left panel for comparison (Ref. 29).

rameters V_S vary only slightly. Since we have employed an effective interaction model, the resulting model parameters are expected to be temperature and concentration dependent. The weak temperature dependence originates mainly from the thermal lattice expansion, which produces smaller effective interaction parameters for higher temperatures due to the larger distance between the atoms interacting with each other. The effect is slightly more pronounced in the case of $Ni_{55}Pd_{45}$ than for $Ni_{25}Pd_{75}$.

The chemical interaction is short ranged and oscillatory with a positive nearest-neighbor interaction and a negative second-nearest-neighbor interaction. This clearly confirms the existence of ordering fluctuations in the system as it is manifested in the diffuse scattering maxima at {1,1,0} and {3,1,0} positions. Adding additional chemical interaction parameters to the model confirms that longer-ranged chemical interactions are insignificant and do not improve the quality of the fit. The main difference for both temperature series is found in the concentration dependence of the effective interaction parameters. The significant difference for the two concentrations is caused by many-body effects which are not yet explicitly included in our model. In the current model higher-order terms in the cluster expansion are projected onto concentration-dependent effective two-body interactions. The comparison of calculated phonon dispersion relations[29,30] with experimental data from Kamitakahara and Brockhouse[31] also demonstrates that many-body interactions play an important role in the Ni-Pd alloy system.

The long-range tail of the interaction parameters is governed by the contribution from the strain-induced interactions. The strain-induced interactions are determined by the elastic constants and the Kanzaki forces, which are related by Eq. (7). Employing the bulk modulus K, only three independent fit parameters are left in order to describe the strain-induced properties of our samples: φ, c_{12}/c_{11}, and c_{44}/c_{11}. Figure 17 shows the elastic constants c_{11}, c_{12}, and c_{44} for $Ni_{55}Pd_{45}$ and $Ni_{25}Pd_{75}$ determined from the fitting parameters. Analogous to the chemical interaction parameters, the values at different temperatures and different concentrations were determined completely independent from each other using separate experimental data sets. The elastic constants of both alloys display a monotonic decrease with temperature for both concentrations, similar to the pure elements Ni and Pd. The elastic constants determined from the diffuse scattering patterns can be directly compared with values extracted by independent experimental techniques, such as speed-of-sound measurements or inelastic neutron scattering. Unfortunately, for Ni-Pd alloys experimental data are not available in the literature. For comparison we show the results of calculations by Upadhyaya *et al.*[29] for $Ni_{55}Pd_{45}$ at room temperature (symbols with dashed lines in the left panel of Fig. 17). We found excellent agreement for all three elastic constants.

Using the values for the elastic constants displayed in Fig. 17 and Eq. (7) the Kanzaki force parameters ϕ_1 and ϕ_2 can be determined from the fit results as a function of temperature for both concentrations (see Fig. 18). The Kanzaki force in the first shell, ϕ_1, shows the same temperature trend for both concentrations with a difference mainly in the magnitude. The absolute value of the Kanzaki force parameters in

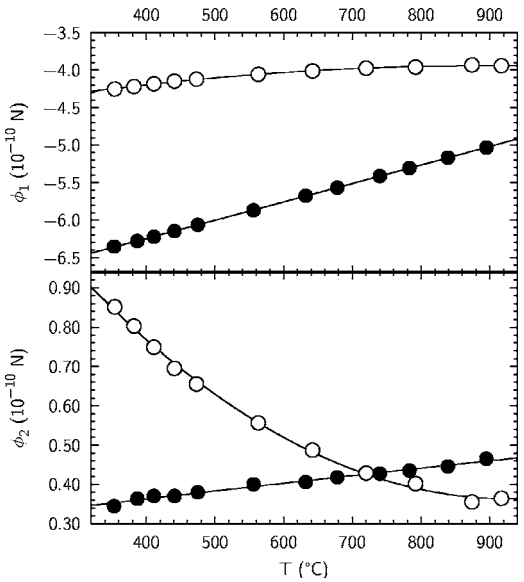

FIG. 18. Temperature dependence of the modulus of the Kanzaki forces ϕ_1 and ϕ_2 (circles) for $Ni_{55}Pd_{45}$ (solid symbols) and $Ni_{25}Pd_{75}$ (open symbols). The lines are a guide for the eye.

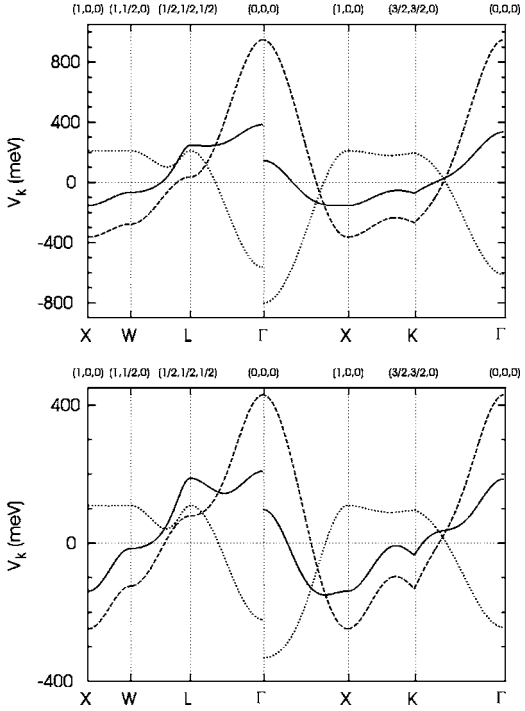

FIG. 19. Effective interaction parameters V_k^{tot} (solid line), V_k^{ch} (dashed line), and V_k^{si} (dotted line) in reciprocal space for $Ni_{55}Pd_{45}$ (top) and $Ni_{25}Pd_{75}$ (bottom) at 410 °C.

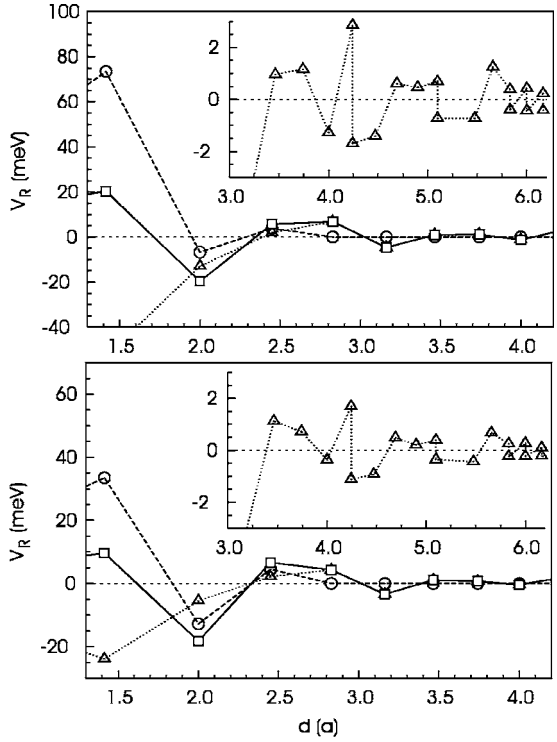

FIG. 20. Effective real-space interaction parameters V_R^{tot} (squares), V_R^{ch} (circles), and V_R^{si} (triangles) for $Ni_{55}Pd_{45}$ (top) and $Ni_{25}Pd_{75}$ (bottom) at 410 °C. The insets magnify the long-range tail of the strain-induced interactions.

the second shell, ϕ_2, is generally an order of magnitude smaller than ϕ_1. This demonstrates that the forces decay rapidly, providing a very compact description of the effects of the size mismatch.

The results for the chemical interaction parameters, the Kanzaki forces, and the elastic constants can now be combined to calculate the chemical, the strain-induced, and the total interaction potential V_k^{tot}. Figure 19 shows the effective interaction parameters in reciprocal space in a reduced Brillouin zone scheme along high-symmetry directions for both concentrations at a temperature of 410 °C. Although both plots exhibit differences in detail, the principal features are very similar. The chemical interactions assume their minimum values at finite wave vectors within the Brillouin zone. This indicates an ordering tendency in the Ni-Pd system. The strain-induced interactions display the opposite behavior with the minimum value at the Γ point indicating a tendency towards phase separation. The sum of both interactions, which constitutes the total effective interaction, is then reflecting the competition between ordering and phase separation. The minimum of V_k^{tot} lies within the Brillouin zone at $\boldsymbol{k}_{\min}=(1,0,0)$, while it is very shallow due to the compensating effect of the strain-induced interaction. This may point to the existence of an ordered ground state, which cannot be reached in the experiment since the system is kinetically frozen at temperatures well above the phase transition temperature. On the other hand, the analysis does not allow one to determine the full Hamiltonian as given by Eq. (3) including $H^{(0)}$ and $V^{\mathrm{ch}(1)}$. The large size mismatch is also producing a pronounced nonanalyticity of V_k^{si} at the Γ point, reflecting the elastic anisotropy of the system. Since the chemical interaction exhibits a pronounced maximum in the Γ-point region, the phase-separating strain-induced interactions are overcompensated.

All the features of the interactions discussed above are encoded in the diffuse scattering pattern via Eq. (8), which relates the effective interaction potentials in k space, V_k^{tot}, with the SRO parameters α_k. In general, large values of V_k^{tot} correspond to low diffuse scattering intensities. The minimum of V_k^{tot} produces the peak (1,1,0.045) in the measured diffuse intensity distribution in Fig. 7. Due to the maximum of V_k^{tot} at the Γ point, the nonanalyticity caused by the strain-induced part V_k^{si} of the interactions is not reflected by a correspondingly nonanalytic diffuse scattering pattern (see Fig. 7). This contrasts with the behavior of alloy systems with a stronger tendency towards phase separation and a large size mismatch, such as Cu-Mn (Ref. 8) or Au-Ni (Ref. 7).

We have also calculated the effective real-space interaction parameters V_R^{tot}, which is the more conventional representation of the interaction parameters, using the relation

$$V_R^{\mathrm{tot}} = N^{-1} \sum_{k \in \mathcal{B}} V_k^{\mathrm{tot}} e^{i\boldsymbol{k}\cdot\boldsymbol{R}}. \tag{19}$$

By way of example we show in Fig. 20 the result for $Ni_{55}Pd_{45}$ and $Ni_{25}Pd_{75}$ at 410 °C. Starting with a positive nearest-neighbor interaction $V_{(1,1,0)}^{\mathrm{tot}}$, the interaction parameters display an oscillatory behavior which is typical for systems with an ordering tendency. The effective interaction potential is very similar for both concentrations with the main difference in the nearest-neighbor interaction V_1^{tot}. The long-range tail of the total interactions, which is magnified in the

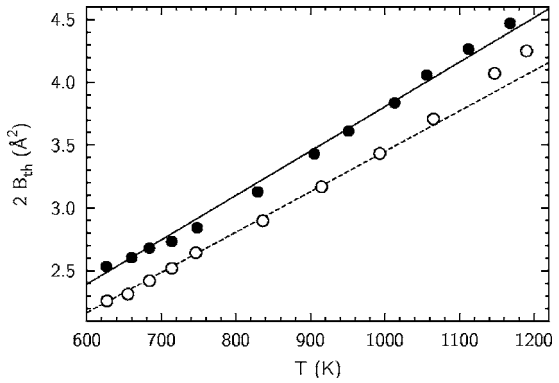

FIG. 21. Temperature dependence of the thermal Debye parameter $2B_{\mathrm{th}}$ for $Ni_{55}Pd_{45}$ (solid circles) and $Ni_{25}Pd_{75}$ (open circles). The lines are calculated using Debye temperatures of $\Theta_D=285$ K and $\Theta_D=275$ K, respectively.

insets of Fig. 20, is entirely determined by the elastic properties of the system. Due to the nonanalyticity of the strain-induced interactions $V_{\boldsymbol{k}}^{\mathrm{si}}$, the total interaction potential $V_{\boldsymbol{R}}^{\mathrm{tot}}$ does not converge in real space, producing a large set of small, but nonvanishing interaction parameters. By employing the Kanzaki force formalism in reciprocal space this tail can be fully described by two Kanzaki coefficients with only the ratio between the Kanzaki force parameters as a free model parameter. The procedure introduced in this work for the analysis of diffuse scattering data from fcc systems demonstrates that the **k**-space approach in combination with a physically motivated interaction model provides a powerful description of binary alloy systems. The values of the interaction energies deduced from our analysis are in good agreement with results from *ab initio* calculations by Paudyal and Mookerjee.[32] In this work the effective nearest-neighbor pair energy was found to be 70.2 meV for $Ni_{50}Pd_{50}$. In addition, their interaction parameters exhibit oscillatory behavior. From the topology of the effective total **k**-space interactions, it is possible to estimate the (coherent) spinodal temperature

$$T_0 \approx -\frac{c(1-c)}{k_{\mathrm{B}}} \min_{\boldsymbol{k}\in\mathcal{B}} V_{\boldsymbol{k}}^{\mathrm{tot}}, \tag{20}$$

where the system undergoes a phase transition from the disordered high-temperature state into a structure characterized by $\boldsymbol{k}_{min}$. Using the parameters determined at 410 °C we can estimate T_0 for the systems $Ni_{55}Pd_{45}$ and $Ni_{25}Pd_{75}$ and find 180 °C and 50 °C, respectively. Both temperatures fall into a regime where the systems are kinetically frozen.

The last model parameter which can be determined directly from the experimentally measured diffuse scattering patterns is the thermal Debye parameter $2B_{\mathrm{th}}$. Figure 21 displays the Debye parameter which exhibits an almost linear increase as a function of temperature. The Debye temperature Θ_D can then be determined from a fit of the thermal Debye parameter $2B_{\mathrm{th}}$ (lines in Fig. 21).[16] We find $\Theta_D=285$ K for $Ni_{55}Pd_{45}$ and $\Theta_D=275$ K for $Ni_{25}Pd_{75}$, respectively. As expected the Debye temperature is larger for the alloy with the higher concentration of heavier Pd atoms. The value for $Ni_{55}Pd_{45}$ can be compared with the value of $\Theta_D=335$ K found by Upadhyaya *et al.*[29]

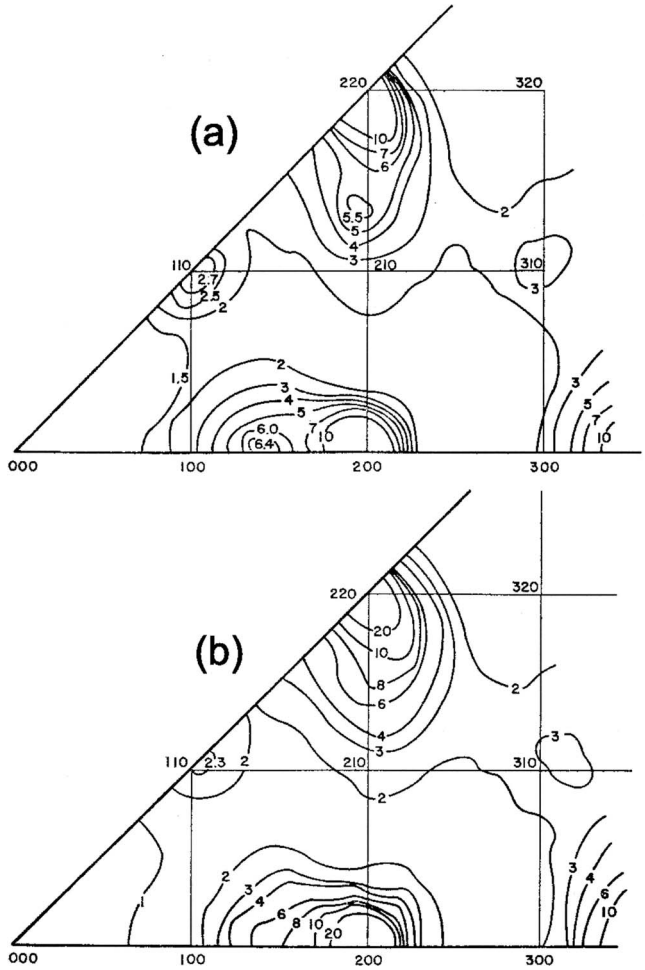

FIG. 22. Diffuse diffraction pattern of (a) $Ni_{50}Pd_{50}$ and (b) $Ni_{25}Pd_{75}$ at room temperature taken from Lin and Spruiell (Ref. 33).

VII. DISCUSSION

Employing our scheme for evaluating diffuse scattering data we have successfully extracted effective interaction potentials as well as thermal and elastic properties for the alloy system Ni-Pd. We have derived a consistent set of parameters such as the thermal Debye parameters, the elastic constants, and the Kanzaki forces induced by the size mismatch between Ni and Pd. Our results can be compared with results from earlier diffuse x-ray scattering experiments by Lin and Spruiell on quenched $Ni_{1-c}Pd_c$ samples[33] performed at a Cu $K\alpha$ source, where the individual components of the diffuse scattering were analyzed by a linear separation technique (see Fig. 22). While we find qualitative agreement in the principal features of the diffuse intensity distributions, it is not possible to compare the results more quantitavely as the samples used by Lin and Spruiell have not been measured in an equilibrium state. In addition, the large value $\alpha_{000}=1.533$ in their analysis indicates that the data set is not consistent. Table IV lists our results for the real-space SRO

TABLE IV. SRO parameters α_{hkl} for $Ni_{55}Pd_{45}$ and $Ni_{55}Pd_{45}$ at two different temperatures. For comparison the results from Lin and Spruiell (Ref. 33) are listed.

			$Ni_{25}Pd_{75}$		$Ni_{55}Pd_{45}$		Lin71
h	*k*	*l*	410 °C	790 °C	410 °C	780 °C	25 °C
0	0	0	1.0000	1.0000	1.0000	1.0000	1.533
1	1	0	−0.0250	−0.0202	−0.0643	−0.0478	0.005
2	0	0	0.0574	0.0299	0.0954	0.0545	0.184
2	1	1	−0.0231	−0.0070	−0.0259	−0.0104	−0.069
2	2	0	−0.0024	−0.0074	0.0042	−0.0042	−0.012
3	1	0	0.0107	0.0067	0.0117	0.0070	0.021
2	2	2	−0.0043	−0.0023	−0.0011	−0.0016	−0.030
3	2	1	−0.0015	−0.0012	−0.0013	−0.0009	−0.010
4	0	0	0.0044	0.0012	0.0064	0.0014	0.013
3	3	0	0.0004	−0.0026	0.0004	−0.0022	−0.005
4	1	1	−0.0002	0.0017	−0.0029	0.0007	−0.006
4	2	0	0.0020	0.0015	0.0026	0.0015	−0.009
3	3	2	−0.0004	−0.0009	−0.0006	−0.0008	−0.005
4	2	2	−0.0004	−0.0004	−0.0003	−0.0003	−0.003
4	3	1	−0.0006	−0.0005	−0.0010	−0.0005	−0.002
5	1	0	0.0006	0.0007	0.0012	0.0007	
5	2	1	0.0003	0.0006	0.0003	0.0005	
4	4	0	−0.0005	−0.0010	−0.0006	−0.0008	−0.015
4	3	3	−0.0004	−0.0005	−0.0006	−0.0004	0.000
5	3	0	0.0004	0.0003	0.0006	0.0003	
4	4	2	−0.0005	−0.0004	−0.0007	−0.0004	0.007

parameters for $Ni_{50}Pd_{50}$ and $Ni_{25}Pd_{75}$ at two temperatures together with earlier results for $Ni_{50}Pd_{50}$.[33]

The positive value of the nearest-neighbor effective pair interaction parameter and the location of the absolute minimum of $V_{\boldsymbol{k}}^{\mathrm{tot}}$ at $\boldsymbol{k} \neq 0$ (see Fig. 19) clearly indicates dominating ordering fluctuations in the Ni-Pd alloy system. Since it is not possible to determine the full Hamiltonian including the dispersion-free interaction parameters $H^{(0)}$ and $V^{ch(1)}$ from diffuse scattering maps [see Eq. (3)], the phase stability cannot be further evaluated at this point.[5] Recent first-principles calculations[34] have shown that the tendency towards phase separation, indicated by a positive formation enthalpy in the Ni-Pd system, is explained by only a small reduction of the size mismatch by relativistic effects as compared to $3d$-$5d$ compounds such as Ni-Pt.

In this work we have combined an experimental technique with methods for quantitative data analysis. The biggest advantage of the high-energy transmission measurement of diffuse intensity distributions is that the resulting data sets are intrinsically consistent. One of the major problems of conventional experimental strategies employing point detectors and reflection geometry with lower-energy x rays is that the experimental conditions are often not stable over the time scales required for diffuse scattering measurements. In addition a number of significant corrections are necessary to produce data sets normalized in absolute units which are self-consistent.

These problems do not arise in high-energy transmission measurements. All data points are measured with the same primary beam from the same sample volume at the same time. Therefore, it is not necessarry to normalize the measured data sets in absolute units in order to retrieve interaction energies which are self-consistent. Another important point is that the measurement of a single 2D diffuse scattering pattern in a single orientation allows us to retrieve 3D information due to the residual curvature of the Ewald sphere. Prior to working with single diffuse scattering patterns for the analysis described in this work, it is therefore mandatory to exploit reciprocal space especially in the high-symmetry planes in order to chose a plane containing the relevant information.

X-ray energies of approximately 100 keV are an ideal probe for most alloy samples. On the other hand, the high energy of the primary beam does not allow one to tune the x-ray energy such as to exploit the anomalous dispersion of the form factors. It is, therefore, not possible to change the ratio between TDS, SRO scattering, and distortion-induced scattering. This has been successfully achieved by the so-called 3λ method for the determination of individual atomic displacements.[35,36]

The results of this work demonstrate that high-quality diffuse scattering data sets can be quantitatively measured on drastically reduced time scales. This enables us to investigate entire phase diagrams as a function of concentration and temperature.

ACKNOWLEDGMENTS

We would like to thank R. Henes (MPI for Metals Research, Stuttgart) for growing the single crystals. We also thank A. Major (Vienna) for his help with the installation of the computing facility used in this work.

APPENDIX: GREEN'S TENSOR AND KANZAKI FORCES

The components of the Green's tensor can be represented as[3]

$$\mathsf{G}_{\boldsymbol{k}}^{ij} = \sum_{\alpha=1}^{3} \frac{e_{\alpha\boldsymbol{k}}^{i} e^{j*}_{\alpha\boldsymbol{k}}}{m\omega_{\alpha\boldsymbol{k}}^{2}} \quad (\boldsymbol{k} \neq 0), \tag{A1}$$

where m is the mass of a host atom, $\omega_{\alpha\boldsymbol{k}}$ is a frequency of the vibration mode $(\alpha\boldsymbol{k})$, and $e_{\alpha\boldsymbol{k}}$ the polarization vector of the branch α. The dispersion $\omega_{\alpha\boldsymbol{k}}$ for the high-symmetry directions in reciprocal space can be determined, e.g., by inelastic neutron diffraction. Then the Green's tensor can be described in terms of the Born–von-Karman constants derived from a model of the lattice dynamics. In its simplest form[1] $\mathsf{G}_{\boldsymbol{k}} = \mathsf{A}_{\boldsymbol{k}}^{-1}$ is represented in terms of the elastic constants c_{ij}. The individual components are then given by

$$\mathsf{A}_{\boldsymbol{k}}^{xx} = ac_{11}\left[2 - \cos\frac{a}{2}k_x\left(\cos\frac{a}{2}k_y + \cos\frac{a}{2}k_z\right)\right] + a(2c_{44} - c_{11})\left(1 - \cos\frac{a}{2}k_y\cos\frac{a}{2}k_z\right),$$

$$\mathsf{A}_{\boldsymbol{k}}^{xy} = a(c_{12} + c_{44})\sin\frac{a}{2}k_x\sin\frac{a}{2}k_y. \tag{A2}$$

The other components of the Green's tensor can be deduced from Eq. (A2) by cyclic permutation. The Fourier components of the Kanzaki forces are given by

$$\phi_{\boldsymbol{k}} = \boldsymbol{a}_{\boldsymbol{k}}^{(1)}\phi_1 + \boldsymbol{a}_{\boldsymbol{k}}^{(2)}\phi_2, \tag{A3}$$

with the geometry factors

$$\boldsymbol{a}_{\boldsymbol{k}}^{(1)} = 2\sqrt{2}\begin{pmatrix} \sin\frac{a}{2}k_x\left(\cos\frac{a}{2}k_y + \cos\frac{a}{2}k_z\right) \\ \sin\frac{a}{2}k_y\left(\cos\frac{a}{2}k_z + \cos\frac{a}{2}k_x\right) \\ \sin\frac{a}{2}k_z\left(\cos\frac{a}{2}k_x + \cos\frac{a}{2}k_y\right) \end{pmatrix}, \tag{A4a}$$

$$\boldsymbol{a}_{\boldsymbol{k}}^{(2)} = 2\begin{pmatrix} \sin ak_x \\ \sin ak_y \\ \sin ak_z \end{pmatrix}. \tag{A4b}$$

The moduli of the Kanzaki forces ϕ_i in the first two coordination shells are given by (see Fig. 18)

$$\phi_1 = \frac{La2(c_{11} + 2c_{12})}{8(\sqrt{2} + \varphi)}, \tag{A5a}$$

$$\phi_2 = \phi_1\varphi, \tag{A5b}$$

where $\varphi = \phi_2/\phi_1$ denotes the constant used for fitting the ratio of the Kanzaki coefficients.

*Electronic address: mezger@mf.mpg.de

†Electronic address: reichert@mf.mpg.de

[1] M. A. Krivoglaz, *X-Ray and Neutron Diffraction in Nonideal Crystals* (Springer, Berlin, 1996).

[2] M. Krivoglaz, *Diffuse Scattering of X-Rays and Neutrons by Fluctuations* (Springer, Berlin, 1996).

[3] A. G. Khachaturyan, *Theory of Structural Transformations in Solids* (Wiley, New York, 1983).

[4] S. Curtarolo, D. Morgan, and G. Ceder, CALPHAD: Comput. Coupling Phase Diagrams Thermochem. **29**, 163 (2005).

[5] C. Wolverton and A. Zunger, Comput. Mater. Sci. **8**, 107 (1997).

[6] C. Wolverton, V. Ozolins, and A. Zunger, J. Phys.: Condens. Matter **12**, 2749 (1999).

[7] H. Reichert *et al.*, Phys. Rev. Lett. **95**, 235703 (2005).

[8] H. Reichert *et al.*, Phys. Rev. Lett. **87**, 236105 (2001).

[9] V. N. Bugaev *et al.*, Phys. Rev. B **65**, 180203(R) (2002).

[10] W. Schweika, *Disordered Alloys* (Springer, Berlin, 1998).

[11] D. de Fontaine, Solid State Phys. **34**, 73 (1979).

[12] H. Kanzaki, J. Phys. Chem. Solids **2**, 24 (1957).

[13] R. Brout, *Phase Transitions* (Benjamin, New York, 1965).

[14] A. Udyansky *et al.*, Phys. Rev. B **71**, 140201(R) (2005).

[15] L. Reinhard and S. C. Moss, Ultramicroscopy **52**, 223 (1993).

[16] J. Als-Nielsen and D. McMorrow, *Elements of Modern X-Ray Physics* (Wiley, Chichester, 2001).

[17] F. Heinrich, Z. Anorg. Chem. **83**, 322 (1913).

[18] W. Fraenkel and A. Stern, Z. Anorg. Chem. **166**, 161 (1927).

[19] V. Marain, Ann. Phys. (Paris) **7**, 459 (1937).

[20] H. Fujiwara, H. Kadomatsu, and K. Ohishi in *Proceedings of the Fourth International Conference on High Pressure*, edited by J. Osugi (The Physico-Chemical Society of Japan, Kyoto, 1975).

[21] J. Beille and R. Tournier, J. Phys. F: Met. Phys. **6**, 621 (1976).

[22] S. Yazliev, Russ. J. Inorg. Chem. **5**, 1185 (1960).

[23] R. E. Bingham and C. R. Brooks, J. Phys. Chem. Solids **30**, 2365 (1969).

[24] J. Tomiska, Q. Jiang, and R. Lück, Z. Metallkd. **84**, 755 (1993).

[25] M. I. Pownceby and H. C. O'Neil, Contrib. Mineral. Petrol. **116**, 327 (1993).

[26] L. R. Bidwell and R. Speiser, Acta Crystallogr. **17**, 1473 (1964).

[27] M. Yoshihara and R. B. McLellan, Acta Metall. **33**, 1129 (1985).

[28] L. Ingber, http://www.ingber.com

[29] S. C. Upadhyaya, J. C. Upadhyaya, and R. Shyam, Phys. Rev. B **44**, 122 (1991).

[30] C. M. I. Okoye and S. Pal, Phys. Rev. B **50**, 7147 (1994).

[31] W. A. Kamitaka and B. N. Brockhouse, Phys. Rev. B **10**, 1200 (1974).

[32] D. Paudyal and A. Mookerjee, J. Phys.: Condens. Matter **16**, 5791 (2004).

[33] W. Lin and J. E. Spruiell, Acta Metall. **19**, 451 (1971).

[34] L. G. Wang and A. Zunger, Phys. Rev. B **67**, 092103(R) (2003).

[35] G. E. Ice, C. J. Sparks, A. Habenschuss, and L. B. Shaffer, Phys. Rev. Lett. **68**, 863 (1992).

[36] L. Reinhard *et al.*, Phys. Rev. B **45**, 2662 (1992).